

Cubic magnetocrystalline anisotropy-driven spin reorientation in TmIG detected by spin Hall magnetoresistance

Qinghui Yu(余庆汇), Xue He(贺雪), Yongli Yu(于永利), Xiuqiao Liu(刘修桥), Shilei Ding(丁石磊), and Rui Wu(吴锐)

Citation: Chin. Phys. B, 2026, 35 (**8**): 087202. DOI: 10.1088/1674-1056/ae5a14
http://cpb.iphy.ac.cn; http://iopscience.iop.org/cpb

What follows is a list of articles you may be interested in

Spin-bias-controlled current rectification and negative magnetoresistance in a quantum dot spin transistor

Zhengzhong Zhang(张正中), Han Hu(胡涵), Runze Zhu(朱润泽), Yanzong Wang(王延宗), and Hao Liu(刘昊)
Chin. Phys. B, 2026, 35 (**7**): 077202. DOI: 10.1088/1674-1056/ae1017

Magnon-magnon coupling in noncollinear synthetic antiferromagnets

Tengfei Zhang(张腾飞), Quwen Wang(王曲文), Min Chen(陈敏), Jie Dong(董洁), Qian Zhao(赵乾), Zimu Li(李子木), Qingfang Liu(刘青芳), Jianbo Wang(王建波), and Jinwu Wei(魏晋武)
Chin. Phys. B, 2025, 34 (**5**): 057201. DOI: 10.1088/1674-1056/adb26b

Anisotropic spin transport and photoresponse characteristics detected by tip movement in magnetic single-molecule junction

Deng-Hui Chen(陈登辉), Zhi Yang(羊志), Xin-Yu Fu(付新宇), Shen-Ao Qin(秦申奥), Yan Yan(严岩), Chuan-Kui Wang(王传奎), Zong-Liang Li(李宗良), and Shuai Qiu(邱帅)
Chin. Phys. B, 2024, 33 (**4**): 047201. DOI: 10.1088/1674-1056/ad1e65

High-performance spin-filtering and spin-rectifying effects in Blatter radical-based molecular spintronic device

Chun-Xu Tong(童春旭), Peng Zhao(赵朋), and Gang Chen(陈刚)
Chin. Phys. B, 2023, 32 (**6**): 067202. DOI: 10.1088/1674-1056/acc16d

Spin Seebeck effect and spin Hall magnetoresistance in the Pt/$Y_3Fe_5O_{12}$ heterostructure under laser-heating

Shuanhu Wang(王拴虎), Gang Li(李刚), Jianyuan Wang(王建元), Yingyi Tian(田颖异), Hongrui Zhang(张洪瑞), Lvkuan Zou(邹吕宽), Jirong Sun(孙继荣), Kexin Jin(金克新)
Chin. Phys. B, 2018, 27 (**11**): 117201. DOI: 10.1088/1674-1056/27/11/117201

RAPID COMMUNICATION

Cubic magnetocrystalline anisotropy-driven spin reorientation in TmIG detected by spin Hall magnetoresistance

Qinghui Yu(余庆汇)[1], Xue He(贺雪)[1], Yongli Yu(于永利)[1], Xiuqiao Liu(刘修桥)[1], Shilei Ding(丁石磊)[2,†], and Rui Wu(吴锐)[1,‡]

[1] *Spin-X Institute, School of Physics and Optoelectronics, State Key Laboratory of Luminescent Materials and Devices, and Guangdong–Hong Kong–Macao Joint Laboratory of Optoelectronic and Magnetic Functional Materials, South China University of Technology, Guangzhou* 511442, *China*

[2] *School of Physical and Mathematical Sciences, Nanyang Technological University, Singapore* 637371, *Singapore*

(Received 6 March 2026; revised manuscript received 31 March 2026; accepted manuscript online 1 April 2026)

The precise manipulation and detection of magnetization in magnetic insulators are essential for the development of next-generation spintronic devices. Here, using a heterostructure consisting of a heavy metal and a magnetic garnet thin film, i.e., (111)-oriented Pt/$Tm_3Fe_5O_{12}$ (TmIG), we reconstruct the three-dimensional magnetization reversal trajectory using spin Hall magnetoresistance (SMR). It is found that the SMR signal of the heterostructure exhibits abrupt jumps when the magnetic field is scanned along the out-of-plane direction, and this anomalous phenomenon persists at temperatures below 100 K. By employing a three-dimensional Stoner–Wohlfarth model, we demonstrate that this behavior originates from a discontinuous magnetization trajectory with a unique *3m* symmetry, which is governed by the competition among the cubic magnetocrystalline anisotropy, magnetoelastic anisotropy, and the Zeeman energy. These results provide a novel strategy for detecting three-dimensional magnetization orientation in magnetic insulators and hold the potential to advance the development of low-energy-consumption spintronic devices.

Keywords: spin Hall magnetoresistance, magnetic anisotropy, rare-earth iron garnet, Stoner–Wohlfarth model, spin reorientation

PACS: 72.25.–b, 75.30.Gw, 75.60.Jk, 75.50.Gg

DOI: 10.1088/1674-1056/ae5a14 **CSTR:** 32038.14.CPB.ae5a14

1. Introduction

The electrical manipulation and detection of magnetic order in heavy metal (HM)/magnetic insulator (MI) heterostructures are central to the advancement of low-power spintronic devices.[1,2] In these systems, the interaction between interfacial magnetization and spin currents gives rise to spin Hall magnetoresistance (SMR), enabling the sensitive electrical readout of the magnetization orientation in the adjacent MI layer.[3–5] As a result, SMR has been widely employed to investigate HM/MI systems,[6–11] with a particular focus on HM/yttrium iron garnet ($Y_3Fe_5O_{12}$, YIG)[12–14] and other rare-earth iron garnets (REIG), formed by substituting Y with rare-earth elements,[8,15–18] mainly due to their high Curie temperature, low damping constant, and long spin transport distance.[19–21]

Compared to YIG, $Tm_3Fe_5O_{12}$ (TmIG) exhibits significant magnetic anisotropy, especially magnetoelastic anisotropy, which is considered to be the origin of robust perpendicular magnetic anisotropy (PMA) in TmIG thin films.[22,23] However, the magnetocrystalline anisotropy (MCA) in TmIG thin films has often been considered secondary to magnetoelastic anisotropy,[23,24] and has therefore frequently been neglected due to its relatively small magnitude.

Recently, field-free spin–orbit torque (SOT) switching of magnetization has been achieved by exploiting the intrinsic cubic MCA in (111)-oriented TmIG films with PMA,[25,26] indicating the non-negligible contribution of cubic MCA to the magnetization switching process. This field-free SOT switching arises specifically in (111)-oriented thin films, where the projection of MCA onto the (111) plane exhibits spontaneous mirror-symmetry breaking.[25] This symmetry breaking acts as an azimuth-dependent effective field that theoretically couples the perpendicular reversal with complex in-plane dynamics. However, anomalous Hall effect (AHE) measurements can only probe the out-of-plane component of the magnetization and therefore cannot fully resolve the three-dimensional magnetization state.[5] Thus, reliable detection and reconstruction of three-dimensional magnetization reversal, including both out-of-plane and in-plane magnetization components in REIG thin films, are still lacking. In contrast, SMR enables the reconstruction of three-dimensional magnetization trajectories under a perpendicular magnetic field, thereby allowing direct mapping of the magnetization switching path.

In this work, we investigate the magnetic field depen-

†Corresponding author. E-mail: shilei.ding@ntu.edu.sg

‡Corresponding author. E-mail: ruiwu001@scut.edu.cn

© 2026 Chinese Physical Society and IOP Publishing Ltd. All rights, including for text and data mining, AI training, and similar technologies, are reserved.

dence of SMR in the Pt/(111)-TmIG heterostructure with easy-plane magnetic anisotropy, which is beneficial for continuously tracking the in-plane magnetization during a relatively slow reversal process. The SMR, which is sensitive to the in-plane magnetization, is employed to detect the three-dimensional magnetization reversal. Our transport measurements reveal that the SMR curves exhibit hysteresis and sharp jumps between high- and low-resistance states below 100 K, resembling the tunneling magnetoresistance (TMR) behavior in traditional magnetic tunnel junctions. By employing a three-dimensional Stoner–Wohlfarth (S–W) model, we demonstrate that the out-of-plane mirror-symmetry breaking associated with cubic MCA, together with field-induced in-plane rotation-symmetry breaking, collectively drives spin reorientation, giving rise to the anomalous sharp jumps observed in the SMR. These results clarify the role of cubic MCA in magnetization reorientation within REIG heterostructures.

2. Experimental details

The high-quality single-crystal TmIG thin film was grown on the (111)-oriented GGG substrate by pulsed laser deposition (PLD) using a KrF excimer laser ($\lambda = 248$ nm) from a stoichiometric TmIG target. The film was deposited at a substrate temperature of 670 °C and a laser fluence of 2 J·cm^{-2}. To obtain in-plane magnetic anisotropy (IMA) TmIG films, an oxygen pressure of 15 Pa was adopted, which is lower than the optimal pressure for PMA.[27] After deposition, the film was cooled down to room temperature at a rate of 10 °C/min while maintaining the oxygen pressure. The surface morphology was characterized using an atomic force microscope (AFM) (Bruker, ICON). The magnetic properties and electrical transport properties were measured using a physical properties measurement system (Quantum Design, PPMS Dynacool). For the transport measurements, a 4-nm-thick Pt layer was deposited on the TmIG film in an ultra-high-vacuum magnetron sputtering chamber, and the resulting Pt/TmIG heterostructure was then patterned into 10 μm × 15 μm Hall bars via photolithography. The current channel of the Hall bars was aligned with the $[11\bar{2}]$ direction of the thin film.

3. Results and discussion

The AFM image of the TmIG film reveals an atomically flat surface with a root-mean-square (RMS) roughness of about 0.12 nm (Fig. 1(a)). The in-plane magnetic hysteresis shows a square loop with a high remanence ratio, indicating strong IMA in this sample from 10 K to 300 K (see supplementary materials Section 1). Figure 1(b) shows the representative in-plane (IP) hysteresis loop measured at 80 K, which exhibits a saturation magnetization (M_s) of 96 kA/m. Notably, no magnetic compensation was observed across the entire temperature range (see supplementary Fig. S1), consistent with previous reports.[5,23,28]

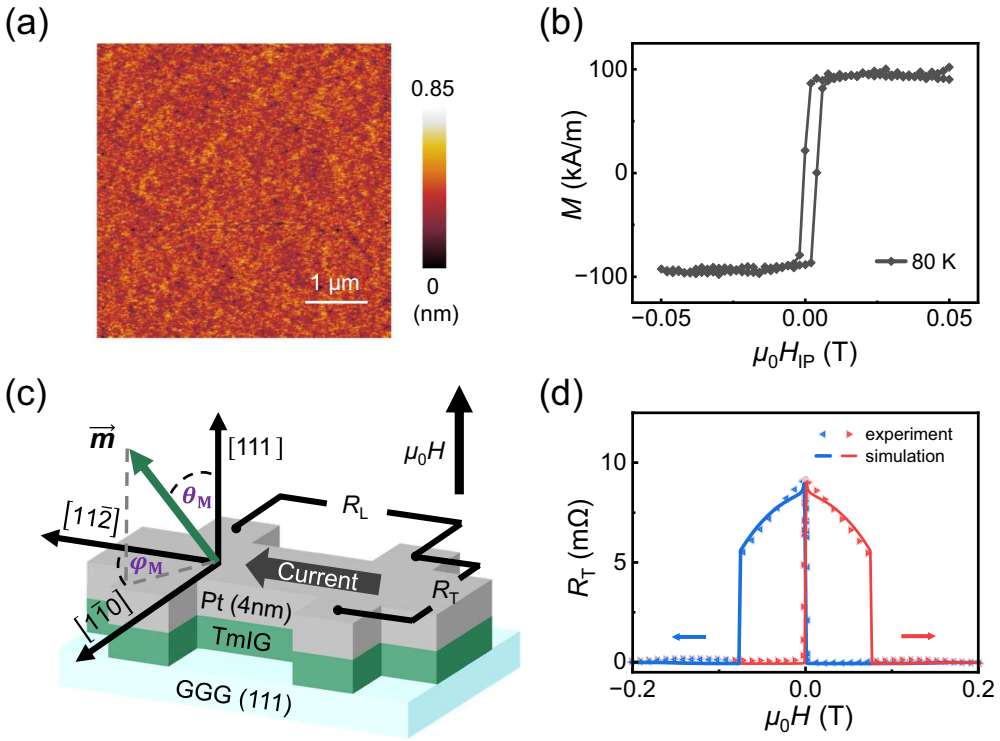


Fig. 1. Characterization of the TmIG film and SMR measurements of the Pt/TmIG heterostructure. (a) AFM image of the TmIG film. (b) Magnetic hysteresis loop of the TmIG thin film measured under an IP magnetic field at 80 K. The paramagnetic contribution from the substrate has been subtracted from the raw data. (c) Schematic of the Pt/TmIG Hall bar device and the electrical transport measurement setup. (d) OOP-field-dependent transverse SMR signal (R_T) measured at 80 K (triangles) together with the simulated curve (solid line). The blue and red arrows indicate the descending and ascending field sweep directions, respectively. The ordinary and anomalous Hall contributions to R_T have been subtracted by symmetrizing the data with respect to the magnetic field.

The measurement schematic is shown in Fig. 1(c), and Fig. 1(d) illustrates the field dependence of the transverse SMR R_T measured at 80 K with a magnetic field applied along the out-of-plane (OOP) direction. The applied current density is fixed at 2×10^6 A·cm^{-2}. The measured R_T shows an anomalous feature that deviates from conventional SMR behavior. Specifically, the curve exhibits a step-like hysteresis loop characterized by sharp transitions between high- and low-resistance states, which resemble the typical characteristics of TMR.[29,30] However, the TMR mechanism can be excluded since our device contains only a single ferromagnetic layer. Furthermore, such step-like features appear in both the transverse and longitudinal channels of the Hall bar. Therefore, we attribute this feature to the abrupt in-plane magnetization reorientation during the reversal process, because both transverse and longitudinal SMR are sensitive to the in-plane components of the magnetization.

To elucidate the anomalous field dependence of SMR, we perform numerical simulations using the three-dimensional S–W model[31] under the coherent rotation assumption. The total energy is given by:[23,25]

$$\begin{aligned} E_{\text{total}} &= K_{c1}F_1(\theta_M,\varphi_M)+K_{c2}F_2(\theta_M,\varphi_M)+K_{u1}\cos^2\theta_M \\ &\quad +K_{u2}\cos^4\theta_M+\frac{\mu_0}{2}M_s^2\cos^2\theta_M-\mu_0M_sH\cos\delta, \quad (1) \end{aligned}$$

where θ_M and φ_M are the polar and azimuthal angles of the magnetization with respect to the $[111]$ and $[11\bar{2}]$ axes, respectively. The parameters $K_{c1,2}$ and $K_{u1,2}$ denote the first- and second-order constants of the cubic MCA and uniaxial magnetoelastic anisotropy, respectively; M_s, H, and δ represent the saturation magnetization, the magnitude of the external field, and the angle between the magnetization and the external field, respectively. It should be noted that a coordinate transformation was performed on the classical cubic MCA formula to unify the angular definitions, yielding the transformed direction cosine polynomials $K_{c1}F_1(\theta_M,\varphi_M)$ and $K_{c2}F_2(\theta_M,\varphi_M)$ (the detailed derivation is provided in supplementary materials Section 2; supplementary Fig. S2 shows the energy landscape of the cubic MCA before and after the coordinate transformation).

Powell's algorithm[32] was used to determine the energy-minimizing equilibrium state (θ_M,φ_M) for each external field H, and the transverse and longitudinal SMR curves were then calculated using:[5,8,12,33]

$$R_T = R_T^{\max}\sin^2\theta\sin2\varphi, \quad (2)$$

$$R_L = R_L^{\max}\sin^2\theta\sin^2\varphi, \quad (3)$$

where θ and φ denote the polar and azimuthal angles of the magnetization with respect to the film normal and the current direction ($\theta=\theta_M$, $\varphi=\varphi_M+\varphi_j$, with φ_j denoting the misalignment angle between the Hall bar channel and the $[11\bar{2}]$ direction), respectively. $R_T^{\max}$ and $R_L^{\max}$ represent the amplitudes of the transverse and longitudinal SMR, respectively.

As shown in Fig. 1(d), the simulated R_T curves at 80 K (solid lines) exhibit excellent agreement with the experimental data. Notably, the simulations accurately reproduce the step-like hysteretic features observed in R_T. This result validates the selected parameters: $K_{c1}=-1.25$ kJ·m^{-3}, $K_{c2}=0.48$ kJ·m^{-3}, $K_{u1}=0.60$ kJ·m^{-3}, $K_{u2}=0.30$ kJ·m^{-3} and $M_s=96.00$ kA·m^{-1}. The negative cubic MCA constant K_{c1} is consistent with the fact that the $\langle111\rangle$ direction serves as the easy magnetization axis in REIG systems.[34] The positive values of $K_{u1,2}$ indicate predominant in-plane compressive strain[35] (as detailed in supplementary materials Section 2), which is consistent with the observed IMA of our TmIG film.

Based on the simulated equilibrium angles (θ_M,φ_M), the spatial trajectory of the magnetization is plotted in Fig. 2(a) (see supplementary Fig. S3 for the field dependence of θ_M and φ_M). This trajectory clearly reveals four in-plane magnetization reorientation events during the entire field sweep, which correspond to the four jumps observed in the SMR signal. Meanwhile, the azimuthal orientations of the magnetization are separated by discrete steps of 60° and 120°, in good agreement with the $3m$ rotational symmetry of the system. In our model, the cubic MCA is the sole energy term that exhibits this specific symmetry in the (111) plane. Therefore, this finding strongly suggests that the cubic MCA is the physical origin of the observed anomalous behavior in the SMR signal.

Figure 2(b) shows the simulated three-dimensional energy distribution of the cubic MCA. In the (111) plane, energy maxima and minima are alternately arranged with intervals of 60°, demonstrating a distinct $3m$ symmetry. Simultaneously, the energy contours display an antisymmetric configuration relative to the equatorial plane with $\theta_M=90°$, where the positions of energy barriers and valleys in the upper and lower hemispheres are distributed in antiphase. This staggered energy landscape imposes strict constraints on the reversal path of the magnetization, preventing it from maintaining a constant azimuthal angle when switching from one pole to the other. This is because the low-energy path initially followed by the magnetization is interrupted by a high-energy barrier upon crossing the equatorial plane. Consequently, driven by the minimization of the total energy, the magnetization must undergo a $\Delta\varphi_M=60°$ azimuthal reorientation upon crossing the equatorial plane to align with an adjacent energy valley. Thus, this specific reorientation process appears as a characteristic sharp jump feature in the SMR measurement. The red arrow in Fig. 2(b) schematically illustrates the trajectory of the magnetization during the ascending field sweep. It can be seen that the trajectory tends to follow the energy valleys of the cubic MCA, where the energy is minimized, indicating that the cubic anisotropy plays a dominant role in determining the in-plane alignment of the magnetization.

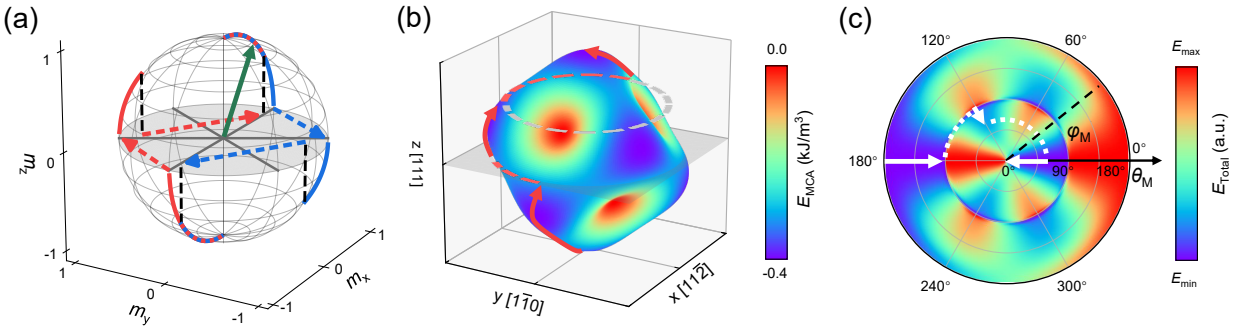


Fig. 2. Magnetization trajectories simulated using the three-dimensional S–W model. (a) Three-dimensional trajectories of the magnetization vector during the magnetic field sweep. The blue and red curves represent the descending and ascending field sweeps, respectively. The equatorial plane ($\theta_M = 90°$) is shaded in gray, with radial lines drawn at 60° intervals. The blue and red dashed arrows indicate the spin reorientation directions. The alternating blue and red lines indicate the overlapping trajectory segments where the descending and ascending paths coincide. (b) Three-dimensional plot of the cubic MCA energy landscape ($K_{c1} = -1.25$ kJ·m^{-3}, $K_{c2} = 0.48$ kJ·m^{-3}). The equatorial plane is shown in gray, and the red arrows schematically illustrate the magnetization trajectory during the ascending field sweep. (c) Polar plot of the relative total energy as a function of φ_M and θ_M during the magnetic field sweep. The polar angle θ_M is linearly mapped to the normalized radial coordinate ($r = \theta_M/180°$), where the center and the perimeter represent $\theta_M = 0°$ and 180°, respectively. For each θ_M, the total energy is calculated over all φ_M values and mapped onto the color scale after normalization.

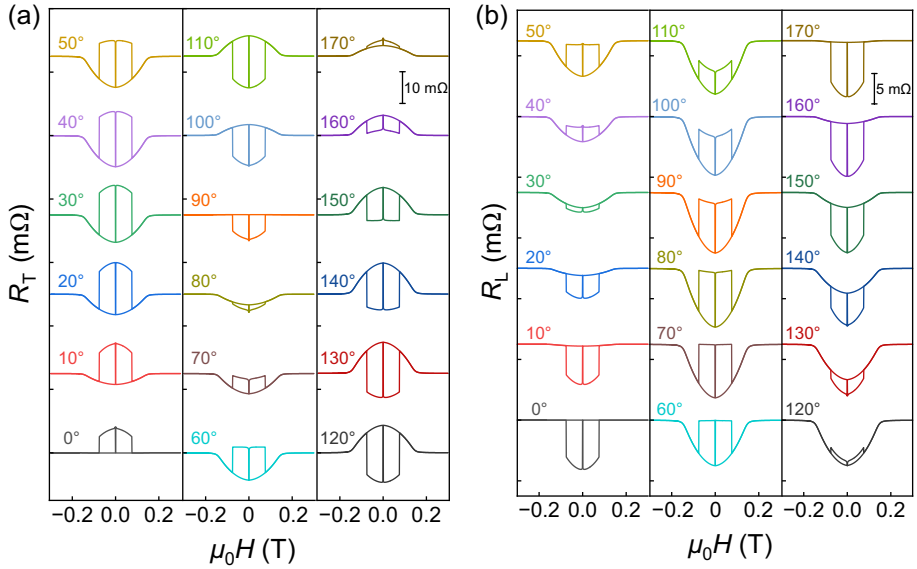


Fig. 3. Simulated current-direction-dependent SMR using the three-dimensional S–W model. (a) Transverse and (b) longitudinal SMR as a function of the OOP magnetic field for different φ_j. The simulation parameters were identical to those at 80 K. The SMR amplitudes were fixed at −10.0 mΩ for comparison.

Theoretically, if the system maintains perfect in-plane $3m$ rotational symmetry, the magnetization would be confined to switching between two adjacent inter-hemispheric energy valleys during the field sweep. Consequently, the magnetoresistance curves would exhibit only two jumps near zero field (see supplementary Fig. S4). However, when the magnetic field applied in the experiment contains a small in-plane component (in our measurements, the external field was tilted by 2° with respect to the [111] direction), it breaks this ideal $3m$ rotational symmetry and lifts the degeneracy of the energy valleys, resulting in secondary switching in the SMR curves.

To reproduce this physical picture in our simulations, we introduced a 2° tilt of the external magnetic field relative to the [111] axis and a 2° azimuthal deviation from the [11$\bar{2}$] axis. We calculated the normalized total energy distribution as a function of the azimuthal angle (φ_M) at each field step. As illustrated in Fig. 2(c), this polar plot intuitively visualizes the evolution of the total energy of TmIG at different azimuthal angles throughout the magnetic field sweep. From the polar plot, six blue and red energy branches arising from the cubic MCA are clearly distinguishable, corresponding to the ⟨111⟩ easy axes and ⟨001⟩ hard axes, respectively. However, it can be clearly observed that the magnetic field component along the x axis (i.e. [11$\bar{2}$]) breaks the rotational symmetry, yielding energy valleys and barriers at $\varphi_M = 0°$ and 180° that are significantly different from those in other directions. During the ascending field sweep, the trajectory of the magnetization orientation (θ_M, φ_M) in the polar energy landscape proceeds slowly from the periphery ($\theta_M = 180°$) toward the center ($\theta_M = 0°$) because the magnetization tends to remain in-plane due to the strong magnetoelastic and shape anisotropy. Driven by energy minimization, the magnetization initially tracks the energy valley along the $\varphi_M = 180°$ direction. However, as the magnetization crosses the equatorial plane into the opposite

hemisphere, the energy landscape is inverted, leading to an abrupt $\Delta\varphi_M = 60^\circ$ jump that switches the magnetization into the adjacent energy valley at $\varphi_M = 120^\circ$. Subsequently, driven by the IP projection of the external field, the magnetization rotates slightly but remains confined within the energy valley at $\varphi_M = 120^\circ$ because the finite field projection is not strong enough to overcome the energy barrier at $\varphi_M = 60^\circ$. As the external field is further increased, the IP projection of the magnetic field further breaks the $3m$ rotational symmetry within the (111) plane, while the OOP projection pulls the magnetization into a canted state. Eventually, the IP component of the external field induces a secondary spin reorientation of $\Delta\varphi_M \approx 120^\circ$ into the energy valley at $\varphi_M = 0^\circ$, while θ_M still changes slowly because the strong easy-plane anisotropy prevents the magnetization from aligning with the OOP direction. This evolution mechanism provides a robust explanation for the sharp-jump signature observed in the field dependence of the SMR.

Moreover, the magnitude of the SMR is determined by the relative angle between the magnetization M and the nonequilibrium spin accumulation σ (which is always perpendicular to the current density j). For the same magnetization reversal, different SMR responses can be obtained by varying the current direction. Thus, we calculated the SMR curves for different current angles φ_j. Notably, as shown in Fig. 3, the curves for the configuration in which the current is not parallel to the $[11\bar{2}]$ axis ($\varphi_j = 0^\circ$) show the typical bell-shaped profile. This smooth resistance variation signifies a coherent rotation of the magnetization from the in-plane to the out-of-plane direction as the Zeeman energy gradually overcomes the strong easy-plane anisotropy. (The result for a current not parallel to the $[11\bar{2}]$ direction is shown insupplementary Fig. S5.)

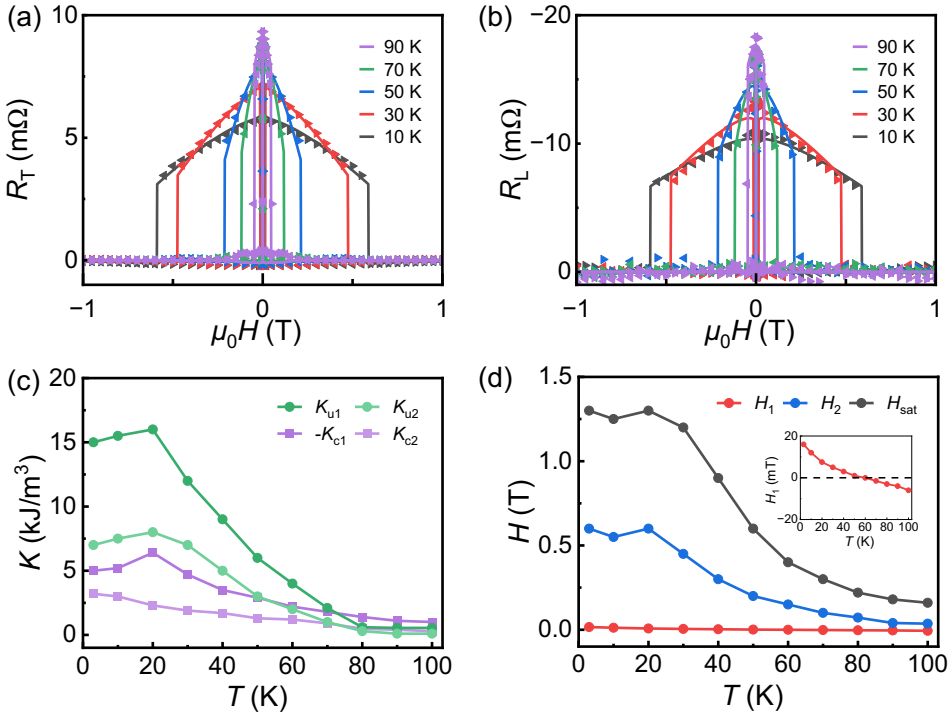


Fig. 4. Temperature-dependent SMR and magnetic parameters. (a) and (b) Experimental data (solid triangles) and S–W model simulations (solid lines) for the transverse and longitudinal SMR from 3 K to 100 K. (c) Temperature-dependent anisotropy constants $K_{c1,2}$ and $K_{u1,2}$ adopted in the simulations. (d) The critical fields for spin reorientation ($H_{1,2}$) and the saturation field (H_{sat}) as functions of temperature. The inset shows an enlarged view of the low-field region.

To further validate the above physical picture, we performed transport measurements over the temperature range from 3 K to 100 K. As shown in Figs. 4(a) and 4(b), both the transverse and longitudinal SMR exhibit hysteretic resistance jumps with opposite jumping directions, and the critical field for the jumps gradually increases as the temperature decreases. The corresponding simulation results are plotted as solid lines in Fig. 4. Notably, the simulations accurately reproduce the temperature-dependent evolution of both the transverse and longitudinal SMR signals, confirming the validity of our model. As illustrated in Fig. 4(c), the cubic MCA constants ($K_{c1,2}$) adopted in the simulations exhibit a gradual increase with decreasing temperature. This behavior is fully consistent with the single-ion model.[36] According to this model, the magnetic anisotropy energy in REIG arises from the combined effects of the crystal and exchange fields on the energy levels of the individual magnetic ions. The Tm^{3+} ions possess unquenched orbital angular momentum, which leads to significant splitting of their energy levels in the crystal field. As thermal fluctuations decrease at low temperatures, the Tm^{3+} ions predominantly occupy their ground states, which are highly anisotropic due to crystal-field inter-

actions. This population effect directly results in a rapid enhancement of the cubic MCA constants. The pronounced increase in the uniaxial anisotropy constants $K_{u1,2}$ with decreasing temperature is primarily attributed to magnetoelastic coupling induced by thermal stress. Magnetoelastic anisotropy is essentially a change in the MCA induced by stress. Thus, it shares the same temperature dependence as the MCA on the one hand, while increasing with increasing stress on the other hand. Since the TmIG film and the GGG substrate possess different thermal expansion coefficients,[23] the thermal stress increases with decreasing temperature. These effects collectively lead to a substantial increase in the easy-plane magnetoelastic anisotropy energy and a corresponding increase in the saturation field.

As shown in Fig. 4(d), both the saturation field and the critical fields of spin reorientation increase with decreasing temperature. The correlated evolution of these fields signifies that the topology of the cubic MCA energy landscape remains invariant across the entire temperature range. This implies that the geometric symmetry of the energy valleys and barriers is preserved despite the enhanced anisotropy, resulting in a proportional scaling of the external fields required for reorientation and saturation.

It is also worth noting that our model elucidates the crystallographic selectivity of this reorientation mechanism: it stems from the broken symmetry of the cubic MCA inherent to (111)-oriented films. Consequently, this mechanism is absent in films epitaxially grown on (110) or (100) substrates,[37] which lack the required energy landscape topology. Finally, we suggest that the analytical framework established herein extends beyond (111)-oriented cubic systems[38,39] and is applicable to rhombohedral or hexagonal systems possessing analogous energy landscapes.[40]

4. Conclusion

In summary, we report an anomalous sharp-jump feature in SMR emerging in (111)-oriented Pt/TmIG heterostructures. By using a three-dimensional Stoner–Wohlfarth model, we successfully determine the complex spin reorientation processes underlying these anomalous SMR signals. Our analysis elucidates how the unique energy landscape of cubic MCA governs the magnetization reversal pathways. Furthermore, we reveal a multiple spin reorientation mechanism driven by the spontaneous mirror-symmetry breaking of cubic MCA, combined with the extrinsic in-plane rotational symmetry breaking induced by the external field. These findings not only demonstrate the significant potential of MCA for manipulating spin states in rare-earth iron garnet systems but also pave the way for the development of novel spin logic and multistate memory devices based on MCA engineering.

Acknowledgments

Project supported by the National Natural Science Foundation of China (Grant No. 12374108), the Guangdong Provincial Quantum Science Strategic Initiative (Grant No. GDZX2401002), and the GJYC program of Guangzhou (Grant No. 2024D01J0087). S.D. acknowledges support from the START-UP GRANT from Nanyang Technological University.

References

[1] Chumak A V, Vasyuchka V I, Serga A A and Hillebrands B 2015 *Nat. Phys.* **11** 453
[2] Shao Q M, Li P, Liu L Q, Yang H, Fukami S, Razavi A, Wu H, Wang K, Freimuth F, Mokrousov Y, Stiles M D, Emori S, Hoffmann A, Akerman J, Roy K, Wang J P, Yang S H, Garello K and Zhang W 2021 *IEEE Trans. Magn.* **57** 1
[3] Chen Y T, Takahashi S, Nakayama H, Althammer M, Goennenwein S T B, Saitoh E and Bauer G E W 2013 *Phys. Rev. B* **87** 144411
[4] Nakayama H, Althammer M, Chen Y T, Uchida K, Kajiwara Y, Kikuchi D, Ohtani T, Geprägs S, Opel M, Takahashi S, Gross R, Bauer G E W, Goennenwein S T B and Saitoh E 2013 *Phys. Rev. Lett.* **110** 206601
[5] Vlietstra N, Shan J, Castel V, Van Wees B J and Ben Youssef J 2013 *Phys. Rev. B* **87** 184421
[6] Althammer M, Meyer S, Nakayama H, Schreier M, Altmannshofer S, Weiler M, Huebl H, Geprägs S, Opel M, Gross R, Meier D, Klewe C, Kuschel T, Schmalhorst J M, Reiss G, Shen L M, Gupta A, Chen Y T, Bauer G E W, Saitoh E and Goennenwein S T B 2013 *Phys. Rev. B* **87** 224401
[7] Isasa M, Bedoya-Pinto A, Vélez S, Golmar F, Sánchez F, Hueso L E, Fontcuberta J and Casanova F 2014 *Appl. Phys. Lett.* **105** 142402
[8] Avci C O, Quindeau A, Pai C F, Mann M, Caretta L, Tang A S, Onbasli M C, Ross C A and Beach G S D 2017 *Nat. Mater.* **16** 309
[9] Hoogeboom G R, Aqeel A, Kuschel T, Palstra T T M and Van Wees B J 2017 *Appl. Phys. Lett.* **111** 052409
[10] Ji Y, Miao J, Zhu Y M, Meng K K, Xu X G, Chen J K, Wu Y and Jiang Y 2018 *Appl. Phys. Lett.* **112** 232404
[11] Fischer J, Althammer M, Vlietstra N, Huebl H, Goennenwein S T B, Gross R, Geprägs S and Opel M 2020 *Phys. Rev. Appl.* **13** 014019
[12] Hahn C, De Loubens G, Klein O, Viret M, Naletov V V and Ben Youssef J 2013 *Phys. Rev. B* **87** 174417
[13] Qu D, Huang S Y, Miao B F, Huang S X and Chien C L 2014 *Phys. Rev. B* **89** 140407
[14] Zhou X, Ma L, Shi Z, Guo G Y, Hu J, Wu R Q and Zhou S M 2014 *Appl. Phys. Lett.* **105** 012408
[15] Dong B W, Cramer J, Ganzhorn K, Yuan H Y, Guo E J, Goennenwein S T B and Kläui M 2018 *J. Phys.: Condens. Matter* **30** 035802
[16] Chen H J, Cheng D S, Yang H L, Wang D K, Zhou S M, Shi Z and Qiu X P 2020 *Appl. Phys. Lett.* **116** 112401
[17] Guo M X, Cheng C K, Liu Y C, Wu C N, Chen W N, Chen T Y, Wu C T, Hsu C H, Zhou S Q, Chang C F, Tjeng L H, Lee S F, Pai C F, Hong M and Kwo J 2022 *Phys. Rev. Mater.* **6** 054412
[18] Cao Van P, Kim H Y, Nguyen Thi T, Duong Viet D, Cao V A, Nah J H, Park S J, Jin H Y, Jo Y H, Park S Y, Park J J, Yuk J M, Kim K J and Jeong J R 2023 *J. Alloys Compd.* **941** 169019
[19] Kajiwara Y, Harii K, Takahashi S, Ohe J, Uchida K, Mizuguchi M, Umezawa H, Kawai H, Ando K, Takanashi K, Maekawa S and Saitoh E 2010 *Nature* **464** 262
[20] Cornelissen L J, Liu J, Duine R A, Youssef J B and Van Wees B J 2015 *Nat. Phys.* **11** 1022
[21] Pirro P, Vasyuchka V I, Serga A A and Hillebrands B 2021 *Nat. Rev. Mater.* **6** 1114
[22] Kubota M, Tsukazaki A, Kagawa F, Shibuya K, Tokunaga Y, Kawasaki M and Tokura Y 2012 *Appl. Phys. Express* **5** 103002
[23] Quindeau A, Avci C O, Liu W Q, Sun C L, Mann M, Tang A S, Onbasli M C, Bono D, Voyles P M, Xu Y B, Robinson J, Beach G S D and Ross C A 2017 *Adv. Electron. Mater.* **3** 1600376

[24] Vu N M, Meisenheimer P B and Heron J T 2020 *J. Appl. Phys.* **127** 153905
[25] Ke J T, Zhang D L, Bi L Z, Li Z L, Zhou S, Wang P J, Zhu Z Z, Bai H, Li G S, Zhu M, Hu C Q, Zhang Y, Liu Y W and Cai J W 2024 *Phys. Rev. Lett.* **133** 186703
[26] Husain S, Prestes N F, Fayet O, Collin S, Godel F, Jacquet E, Denneulin T, Dunin-Borkowski R E, Thiaville A, Bibes M, Jaffrès H, Reyren N, Fert A and George J M 2024 *Nano Lett.* **24** 2743
[27] Liang Z G, Lu J D, Yang S, Fang Z, Yan Y F, Wang Q, Li P, Fan M H and Wang L F 2024 *Adv. Funct. Mater.* **34** 2315147
[28] Hansen P and Tolksdorf W 1991 *J. Appl. Phys.* **69** 4577
[29] Miyazaki T and Tezuka N 1995 *J. Magn. Magn. Mater.* **139** L231
[30] Moodera J S, Kinder L R, Wong T M and Meservey R 1995 *Phys. Rev. Lett.* **74** 3273
[31] Stoner E C and Wohlfarth E P 1948 *Philos. Trans. R. Soc. Lond. Ser. A* **240** 599
[32] Powell M J D 1964 *Comput. J.* **7** 155
[33] Meyer S, Schlitz R, Geprägs S, Opel M, Huebl H, Gross R and Goennenwein S T B 2015 *Appl. Phys. Lett.* **106** 132402
[34] Lee E W 1979 *Phys. Bull.* **30** 533
[35] Fu J B, Hua M X, Wen X, Xue M Z, Ding S L, Wang M, Yu P, Liu S Q, Han J Z, Wang C S, Du H L, Yang Y C and Yang J B 2017 *Appl. Phys. Lett.* **110** 202403
[36] Pearson R F 1962 *J. Appl. Phys.* **33** 1236
[37] Liu Y K, Wong H F, Ng S M, Mak C L and Leung C W 2020 *J. Magn. Magn. Mater.* **501** 166454
[38] Jin L C, Zhang D N, Zhang H W, Tang X L, Bai F M, Zhong Z Y, Fan X and Xiao J Q 2014 *Appl. Phys. Lett.* **105** 132411
[39] Liu Q B, Meng K K, Xu Z D, Zhu T, Xu X G, Miao J and Jiang Y 2020 *Phys. Rev. B* **101** 174431
[40] Tang M, Huang J W, Qin F, Zhai K, Ideue T, Li Z, Meng F H, Nie A M, Wu L L, Bi X Y, Zhang C R, Zhou L, Chen P, Qiu C Y, Tang P Z, Zhang H J, Wan X G, Wang L, Liu Z Y, Tian Y J, Iwasa Y and Yuan H T 2022 *Nat. Electron.* **6** 28